

Large spin Hall conductivity in epitaxial thin films of kagome antiferromagnet Mn_3Sn at room temperature

Himanshu Bangar,¹ Kacho Imtiyaz Ali Khan,¹ Akash Kumar,² Niru Chowdhury,¹ Prasanta Kumar Muduli,³ and Pranaba Kishor Muduli*¹

¹*Department of Physics, Indian Institute of Technology Delhi, Hauz Khas, New Delhi 110016, India.*

²*Department of Physics, University of Gothenburg, 412 96 Gothenburg, Sweden.*

³*Department of Physics, Indian Institute of Technology Madras, Chennai, Tamil Nadu 600036, India.*

(*Electronic mail: muduli@physics.iitd.ac.in)

(Dated: 7 September 2022)

Mn_3Sn is a non-collinear antiferromagnetic quantum material that exhibits a magnetic Weyl semimetallic state and has great potential for efficient memory devices. High-quality epitaxial c -plane Mn_3Sn thin films have been grown on a sapphire substrate using a Ru seed layer. Using spin pumping induced inverse spin Hall effect measurements on c -plane epitaxial $\text{Mn}_3\text{Sn}/\text{Ni}_{80}\text{Fe}_{20}$, we measure spin-diffusion length ($\lambda_{\text{Mn}_3\text{Sn}}$), and spin Hall conductivity (σ_{SH}) of Mn_3Sn thin films: $\lambda_{\text{Mn}_3\text{Sn}} = 0.42 \pm 0.04$ nm and $\sigma_{\text{SH}} = -702 \hbar/e \Omega^{-1}\text{cm}^{-1}$. While $\lambda_{\text{Mn}_3\text{Sn}}$ is consistent with earlier studies, σ_{SH} is an order of magnitude higher and of the opposite sign. The behavior is explained on the basis of excess Mn, which shifts the Fermi level in our films, leading to the observed behavior. Our findings demonstrate a technique for engineering σ_{SH} of Mn_3Sn films by employing Mn composition for functional spintronic devices.

Recently, there has been a huge amount of interest in quantum materials for the field of spintronics, which makes use of the electron's spin degree of freedom.^{1,2} Spin-charge interconversion is important for the application of spintronics. Spin current can be generated from the charge current by a mechanism such as spin Hall effect (SHE), which is typically observed in non-magnetic heavy metals. However, recently non-collinear antiferromagnetic materials have gained attention as potential spin Hall materials. This is driven by (1) theoretical studies that predict large intrinsic spin Hall conductivity (σ_{SH}),^{3,4} (2) the experimental observation of large anomalous Hall effect⁵, and (3) the observation of un-conventional spin-orbit torque⁶ in these materials. Mn_3Sn is one example of non-collinear antiferromagnet that exhibits exotic properties such as anomalous Hall effect,⁵ anomalous Nernst effect,⁷ and magneto-optic Kerr effect,⁸ despite having nearly zero magnetization. These exotic properties originate from the Berry curvature associated with Weyl points near the Fermi energy.^{9,10} More recently, new phenomena such as magnetic spin Hall effect,¹¹ chiral domain walls¹² as well as spin-orbit torque induced chiral-spin rotation¹³ has been demonstrated in Mn_3Sn . These reports suggest that Mn_3Sn is a promising material for antiferromagnetic spintronics; a rapidly developing field that offers several advantages such as zero stray field, robustness against magnetic field perturbation, and ultrafast THz dynamics.^{14,15}

Theoretical works predict an intrinsic σ_{SH} in Mn_3Sn due to its non-collinear magnetic structure.^{3,4,16} Only a few works are reported on the measurement of SHE in Mn_3Sn . The σ_{SH} of polycrystalline Mn_3Sn was recently reported to be $\sigma_{\text{SH}} \sim 47 \hbar/e \Omega^{-1}\text{cm}^{-1}$ based on non-local spin transport experiments.¹⁷ Yu *et al.*¹⁸ reported a spin Hall angle (θ_{SH}) of 0.144 using the spin pumping induced inverse spin Hall effect (ISHE) approach, which is greater than that of Ta. To realize the full potential of Mn_3Sn for spintronics applications, it is important to estimate σ_{SH} as well as other important param-

eters like spin mixing conductance ($g_{\uparrow\downarrow}$), and spin diffusion length ($\lambda_{\text{Mn}_3\text{Sn}}$) in epitaxial thin films. Recently, Yoon *et al.* reported a drastic change in transport properties with the crystalline orientation of Mn_3Sn thin films¹⁹. Theoretical studies also predicts strong anisotropic θ_{SH} for Mn_3Sn .¹⁶ Consequently, it is anticipated that the values of $g_{\uparrow\downarrow}$, $\lambda_{\text{Mn}_3\text{Sn}}$, and σ_{SH} will depend on the orientation of Mn_3Sn thin films.

In this work, we present direct measurement of σ_{SH} in high quality c -plane oriented Mn_3Sn thin films. We grow c -plane oriented Mn_3Sn on Al_2O_3 substrate using Ru as the seed layer. We determine the σ_{SH} by employing spin pumping driven ISHE measurements on *epi*- $\text{Mn}_3\text{Sn}/\text{Ni}_{80}\text{Fe}_{20}$ bilayers. In contrast to previously reported investigations, σ_{SH} of our epitaxial Mn_3Sn thin films is an order of magnitude greater, while $\lambda_{\text{Mn}_3\text{Sn}}$ is comparable. We also report $g_{\uparrow\downarrow}$ of this system to be $(1.54 \pm 0.27) \times 10^{19} \text{ m}^{-2}$, which is also an order of magnitude higher compared to Py/Ta bilayers.^{20,21} The sign of σ_{SH} is found to be negative, which can be explained by a shift of the Fermi level caused by a slight excess of Mn in our films.

Mn_3Sn has a hexagonal crystal structure, for which the (0001)-plane or the c -plane has a kagome lattice as shown in Fig. 1(a). In order to grow the c -plane Mn_3Sn , we choose c -plane sapphire ($c\text{-Al}_2\text{O}_3$) substrate and a 7 nm thick Ru-seed layer. The films were grown using AJA Orion 8 magnetron sputtering system with a base pressure, better than 5×10^{-8} Torr. First, the Ru seed layer was deposited at 400 °C and annealed at the same temperature for 10 minutes. Then the sample was allowed to cool to 100 °C, at which Mn_3Sn was deposited by co-sputtering Mn and Sn targets. The Mn was deposited at a growth rate of 0.37 Å/s by applying 60 W DC power while the Sn was deposited at a growth rate of 0.20 Å/s by applying 40 W RF power. After the deposition of Mn_3Sn layer, the sample was annealed *in-situ* at 600 °C for an hour. Subsequently, the sample was allowed to cool to room temperature, after which $\text{Ni}_{80}\text{Fe}_{20}$ (8 nm)/Al (2 nm) was deposited without breaking the vacuum. The Al layer is used

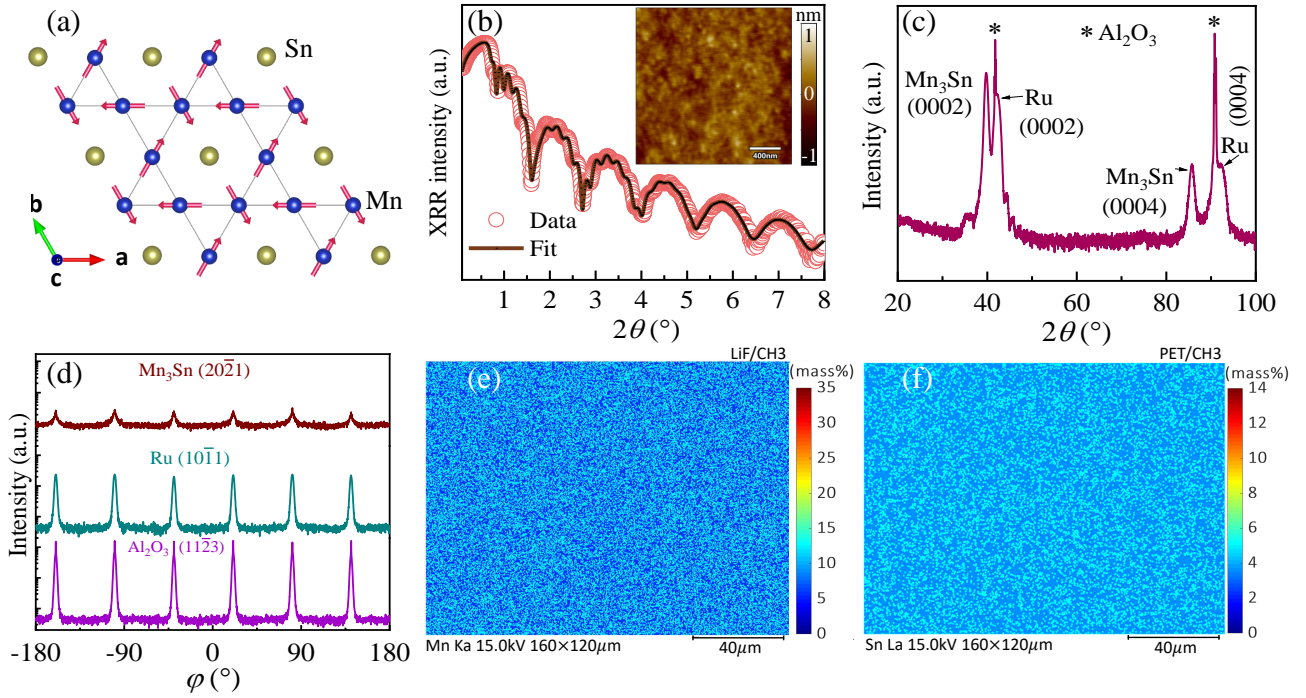


FIG. 1. (a) The magnetic and crystal structure of c -plane Mn_3Sn , revealing the kagome lattice of Mn magnetic moments. (b) Measured X-ray reflectivity (red circles) for the $\text{Ru}(7\text{ nm})/\text{Mn}_3\text{Sn}(30\text{ nm})/\text{AlO}_x(2\text{ nm})$ thin film and corresponding theoretical fit (black solid line). Inset: the surface topography of the same sample measured using AFM. The scan area is $2\ \mu\text{m} \times 2\ \mu\text{m}$. (c) X-ray diffraction (XRD) spectra for the $\text{Ru}(7\text{ nm})/\text{Mn}_3\text{Sn}(30\text{ nm})/\text{AlO}_x(2\text{ nm})$ thin film. (d) The corresponding ϕ -scan for Al_2O_3 ($11\bar{2}3$) (violet), Ru ($10\bar{1}1$) (cyan) and Mn_3Sn ($20\bar{2}1$) (wine). Elements distribution maps for (e) Mn and (f) Sn measured using electron probe microanalyzer (EPMA).

as the capping layer and is fully oxidized after exposure to air. During the deposition, we rotate the sample holder along its normal axis to ensure a uniform composition and thickness. The structural characterization was performed using high resolution X-ray diffraction (HR-XRD), while the growth rate and interfacial roughness were determined via X-ray reflectivity (XRR) measurements using a PANalytical x-ray diffractometer equipped with $\text{Cu K}\alpha$ ($\lambda = 1.5406\ \text{\AA}$) source. The morphology and surface roughness was determined by atomic force microscopy (AFM) scans (Asylum Research, MFP-3D system). The AFM images were obtained in the tapping mode using Asylum Research Probes (AC240TS-R3) cantilevers. The SHIMADZU (EPMA -1720 HT) electron probe microanalyzer (EPMA) system was used to determine the composition. A broadband ferromagnetic resonance (FMR) spectroscopy technique was used to characterize the magnetization dynamics of $\text{Mn}_3\text{Sn}/\text{Ni}_{80}\text{Fe}_{20}$ bilayers. Field modulation technique with lock-in based detection is employed to enhance the sensitivity of FMR measurements.²² The excitation radio frequency (RF) was varied from 3 to 8 GHz. To detect the ISHE voltage, copper pads were pasted beneath the inverted sample following the method used in our earlier work by Kumar *et al.*²⁰

Figure 1(b) shows the XRR measurement of the $\text{Al}_2\text{O}_3/\text{Ru}(7\text{ nm})/\text{Mn}_3\text{Sn}(30\text{ nm})/\text{AlO}_x(2\text{ nm})$ thin film. The thickness of Mn_3Sn is extracted from the XRR fit, from which we determine the growth rate to be $\approx 0.48\ \text{\AA}/\text{s}$. We obtained a low roughness ($\approx 0.28\text{ nm}$) from the fit of the XRR data.

The AFM surface morphology also showed a lower root mean square roughness of $\approx 0.15\text{ nm}$ measured over a scan area of $2\ \mu\text{m} \times 2\ \mu\text{m}$ as shown in the inset. Figure 1(c) shows the corresponding 2θ - θ XRD pattern, showing the (0002)-peaks corresponding to both Mn_3Sn and Ru seed layer. We also observe several satellite peaks (thickness fringes), indicating smooth interfaces and uniform film growth, which is also consistent with sharp Kiessig fringes observed in the XRR measurements [Fig. 1(b)]. We only observed (0002) and (0004) Mn_3Sn peaks, indicating that a c -plane oriented epitaxial Mn_3Sn film has been achieved on the Ru seed layer. To determine the epitaxial relationship, we performed ϕ -scans for the peaks: Al_2O_3 ($11\bar{2}3$) (violet), Ru ($10\bar{1}1$) (cyan) and Mn_3Sn ($20\bar{2}1$) (wine) as presented in Fig. 1(d). The ϕ -scan clearly shows that a reflection appears periodically every 60° for Al_2O_3 , Ru, and Mn_3Sn , indicating that we have obtained non-twinned, highly epitaxial films. The location of the peaks indicates that the epitaxial film is formed with a relationship of Mn_3Sn (0001)[$20\bar{2}0$] \parallel Ru (0001)[$10\bar{1}0$] \parallel Al_2O_3 (0001)[$11\bar{2}0$], which is similar to the work by S. Kurdi *et al.*²³

In order to determine the composition and its distribution, we used an electron probe microanalyzer (EPMA) and energy dispersive X-ray (EDX) mapping on our samples. The composition of the film is estimated to be $\text{Mn}_{3.14\pm 0.03}\text{Sn}_{0.86\pm 0.01}$ using EDX mapping and $\text{Mn}_{3.12\pm 0.02}\text{Sn}_{0.88\pm 0.01}$ by quantitative analysis using EPMA system. Both measurements show the presence of excess Mn, which is known to be essential for the formation of the D0_{19} Mn_3Sn .²⁴ Figure 1(e) and (f)

provide the elemental distribution maps of Mn and Sn atoms, respectively, showing that the elements are uniformly distributed. We measured the longitudinal resistivity of Ru(7 nm)/Mn₃Sn(30 nm) bilayer using four point probe method to be 570 $\mu\Omega\text{-cm}$.

Magnetization (M) measurement performed using superconducting quantum interference device (SQUID) on a 30 nm thick Mn₃Sn thin film is shown in Fig. 2(a). It shows a weak magnetic moment of around 2 $m\mu_B/\text{Mn}$ at room temperature, which is lower than polycrystalline films, as well as reported results on c -plane Mn₃Sn thin films.^{24,25} Magnetization (M) measurement for Mn₃Sn/Ni₈₀Fe₂₀ (8 nm) bilayer is shown in the inset of Fig. 2(a), from which we determine saturation magnetization of Ni₈₀Fe₂₀ to be 750 emu/cc. In Fig. 2(b), we show example FMR spectra of Al₂O₃/Ru/Mn₃Sn($t_{\text{Mn}_3\text{Sn}}$)/Ni₈₀Fe₂₀/AlO_x for various thicknesses, $t_{\text{Mn}_3\text{Sn}}$ of Mn₃Sn measured at 4 GHz. The FMR data is fitted²⁶ to extract the values of half-width at half maximum (HWHM) or linewidth (ΔH) and resonance field (H_r).

The ΔH vs. frequency (f) dependence of all the samples are plotted in Fig. 2(c). The measured data is fitted using following equation:

$$\Delta H = \frac{2\pi\alpha_{\text{eff}}f}{\gamma} + \Delta H_0, \quad (1)$$

where α_{eff} is the effective Gilbert damping parameter, $\gamma = 1.85 \times 10^2$ GHz/T is the gyromagnetic ratio, and ΔH_0 is the inhomogeneous line broadening. The first term on the right hand side is the viscous damping of magnetization motion, while the second term is due to magnetic inhomogeneity and sample imperfections of the FM layer.²⁷ The slope of the linear fit using Eq. 1 is proportional to α_{eff} . As can be observed from Fig. 2(c), the slope of Mn₃Sn($t_{\text{Mn}_3\text{Sn}}$)/Ni₈₀Fe₂₀(8 nm) is higher compared to its corresponding reference Ni₈₀Fe₂₀(8 nm) sample, which indicates spin current being pumped from Ni₈₀Fe₂₀ into Mn₃Sn. Further, the low values of ΔH_0 (< 3 Oe) from the fits indicate the high quality of our samples. Figure 2(d) shows the f dependent H_r (open circles) for various $t_{\text{Mn}_3\text{Sn}}$ with their corresponding fit (solid line) using Kittel's equation:²⁸

$$f = \frac{\gamma}{2\pi} [(H_r + H_k)(H_r + H_k + 4\pi M_{\text{eff}})]^{1/2}, \quad (2)$$

where H_k is the uniaxial anisotropy field, and M_{eff} is the effective saturation magnetization. The M_{eff} is found to be comparable for all the Mn₃Sn($t_{\text{Mn}_3\text{Sn}}$)/Ni₈₀Fe₂₀ samples and in the range of 740 – 770 emu/cc, which is close to measured saturation magnetization of 750 emu/cc (estimated from magnetization measurements), indicating negligible perpendicular anisotropy.

Next, we performed the Mn₃Sn thickness dependent ISHE measurements to determine the θ_{SH} of our c -plane Mn₃Sn films. Figure 2(e) shows a representative ISHE signal, V_{ISHE} (open circles) along with an ISHE signal measured from a Ta/Py/SiO₂ sample (inset). To eliminate contribution from self-induced ISHE and other rectification effects from

Ni₈₀Fe₂₀^{29–31}, the signal from a reference (Ni₈₀Fe₂₀) sample is subtracted from the measured data. The sign of signal obtained from Mn₃Sn agrees with Ta, indicating a negative sign of θ_{SH} . The ISHE data (V_{ISHE}) was fitted with a combination of symmetric ($V_{\text{ISHE}}^{\text{sym}}$) and asymmetric ($V_{\text{ISHE}}^{\text{asym}}$) components using equation:³²

$$V_{\text{ISHE}} = V_{\text{ISHE}}^{\text{sym}} \frac{(\Delta H)^2}{\Delta H^2 + (H - H_r)^2} + V_{\text{ISHE}}^{\text{asym}} \frac{2\Delta H(H - H_r)}{\Delta H^2 + (H - H_r)^2}, \quad (3)$$

where H is the applied magnetic field. The value of the symmetric part can be taken to be the spin pumping induced ISHE signal ($V_{\text{ISHE}}^{\text{sym}}$) in our geometry where rectification signals are minimized.²⁰ This is further supported by the fact that signal shape is entirely symmetric and the signal changes sign on reversal of field polarity, both of which are consistent with a dominant ISHE origin of the signal.³³ Furthermore, in our geometry the magnetic field is perpendicular to the voltage measurement direction. For this condition, the magnetic spin Hall effect vanishes completely [see Fig. 3 (g) of Ref.11]. Hence, in the following, we will not consider magnetic spin Hall effect or it's inverse in Mn₃Sn. The charge current generated due to ISHE in Mn₃Sn can be written as $V_{\text{ISHE}}^{\text{sym}}/R$, where R is the resistance of the Mn₃Sn/Ni₈₀Fe₂₀ bilayer. We further normalize the $V_{\text{ISHE}}^{\text{sym}}/R$ with the width (w) of the sample to eliminate any size effect. In order to determine θ_{SH} and $\lambda_{\text{Mn}_3\text{Sn}}$ of Mn₃Sn we plot $V_{\text{ISHE}}^{\text{sym}}/Rw$ with $t_{\text{Mn}_3\text{Sn}}$ (Fig. 2(f)) and fit it with the following equation:³²

$$\frac{V_{\text{ISHE}}^{\text{sym}}}{Rw} = \theta_{\text{SH}} t_{\text{Mn}_3\text{Sn}} \frac{\hbar g_{\uparrow\downarrow} \gamma^2 h_{\text{RF}}^2 (4\pi M_s \gamma + \sqrt{(4\pi M_s \gamma)^2 + 4\omega^2})}{8\pi \alpha_{\text{eff}}^2 ((4\pi M_s \gamma)^2 + 4\omega^2)} \times \left(\frac{2e}{\hbar} \right) \frac{\lambda_{\text{Mn}_3\text{Sn}}}{t_{\text{Mn}_3\text{Sn}}} \tanh \left(\frac{t_{\text{Mn}_3\text{Sn}}}{2\lambda_{\text{Mn}_3\text{Sn}}} \right), \quad (4)$$

where h_{RF} is the RF field generated due to the RF current of frequency $f = \omega/2\pi$ flowing through the co-planar waveguide, $4\pi M_s$ is the saturation magnetization, \hbar is the reduced Planck's constant, and e is the electronic charge. From the fitting, we obtain the values of $\lambda_{\text{Mn}_3\text{Sn}}$ and θ_{SH} to be 0.42 ± 0.04 nm and -0.40 ± 0.03 , respectively. The $g_{\uparrow\downarrow}$ is determined from the enhancement of damping using $g_{\uparrow\downarrow} = \Delta\alpha_{\text{eff}} 4\pi M_s t_{\text{Py}} / (g\mu_B)$.³⁴ The value is found to be $g_{\uparrow\downarrow} = 1.54 \pm 0.27 \times 10^{19} \text{ m}^{-2}$ at room temperature. This value of $g_{\uparrow\downarrow}$ is comparable to the values reported for other systems such as Mn₃Ga/CoFeB³⁵ and Bi₂Se₃/Ni₈₀Fe₂₀³² and one order of magnitude higher than Ta/Ni₈₀Fe₂₀.²⁰ The value of $\lambda_{\text{Mn}_3\text{Sn}}$ is similar to the value reported for polycrystalline Mn₃Sn.¹⁷ The measured θ_{SH} in our case is found to be rather large, especially considering the fact that Eq. 4 does not include interface transparency, which is less than one. Thus the values of -0.40 ± 0.03 is a lower limit of θ_{SH} . Our value of θ_{SH} is greater than other antiferromagnets, such as $\theta_{\text{SH}} \approx 0.31$ for polycrystalline Mn₃Ga³⁵ and $\theta_{\text{SH}} \approx 0.35$ for (001)-oriented IrMn₃.³⁶ In addition, the observed value of θ_{SH} is considerably higher than

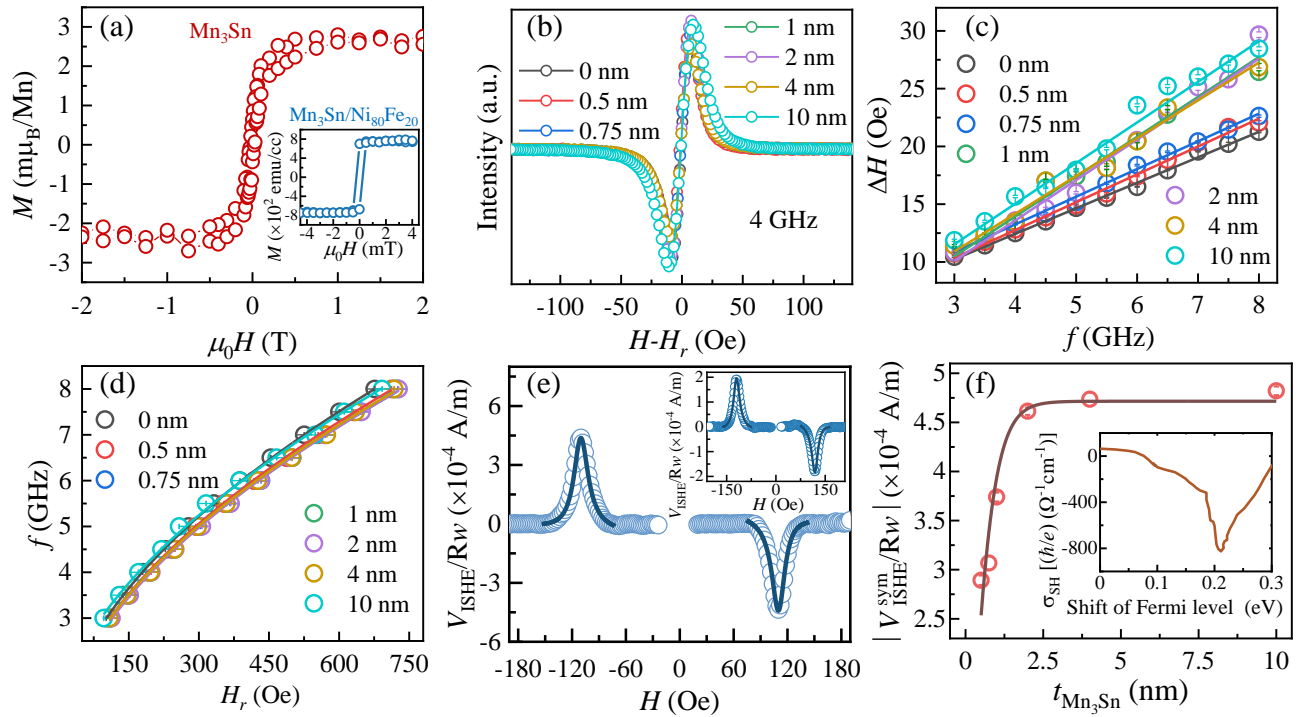


FIG. 2. (a) SQUID magnetization (M) curve of Mn_3Sn (30 nm) sample. Inset: Magnetization (M) curve of Mn_3Sn (30 nm)/ $\text{Ni}_{80}\text{Fe}_{20}$ (8 nm) bilayer thin film. (b) The measured FMR signal at 4 GHz for samples $(\text{Al}_2\text{O}_3/\text{Ru}/\text{Mn}_3\text{Sn}(t_{\text{Mn}_3\text{Sn}})/\text{Ni}_{80}\text{Fe}_{20}/\text{AlO}_x)$ having different thickness, $t_{\text{Mn}_3\text{Sn}}$ of Mn_3Sn near the resonance field (H_r). (c) Linewidth (ΔH) vs. frequency (f) (open circle) and their corresponding fit (solid lines) with Eq. 1. (d) f vs. H_r curve for different $t_{\text{Mn}_3\text{Sn}}$ (open circle) and their corresponding fit (solid lines) with Eq. 2. (e) A representative ISHE signal for $\text{Mn}_3\text{Sn}(10 \text{ nm})/\text{Ni}_{80}\text{Fe}_{20}(8 \text{ nm})$ sample. Inset: ISHE signal for a reference $\text{Ta}(5 \text{ nm})/\text{Ni}_{80}\text{Fe}_{20}(8 \text{ nm})$ bilayer to establish the negative sign of spin Hall conductivity (σ_{SH}) in $\text{Mn}_3\text{Sn}(10 \text{ nm})$. (f) The plot of the ratio $V_{\text{ISHE}}^{\text{sym}}/R_w$ as a function of Mn_3Sn thickness ($t_{\text{Mn}_3\text{Sn}}$) and its fit with Eq. 4 to determine $\lambda_{\text{Mn}_3\text{Sn}}$ and θ_{SH} . The inset depicts the predicted σ_{SH} based on Ref.³, when the Fermi level is moved upward with electron doping *e.g.*, due to high Mn concentration.

the polycrystalline Mn_3Sn value of $\theta_{\text{SH}} \approx 0.05$, which was reported by one of the authors of this article using a non-local spin transport technique.¹⁷ Our value is also more than twice that of Yu *et al.*,¹⁸ where a value of $\theta_{\text{SH}} \approx 0.18$ was reported for polycrystalline Mn_3Sn thin films interfaced with yttrium iron garnet.

In order to compare our results with theoretical calculations³ of SHE in Mn_3Sn , we determine σ_{SH} using: $\sigma_{\text{SH}} = \theta_{\text{SH}} \times \sigma_e^{\hbar}$, where σ is the charge conductivity of $\text{Ru}/\text{Mn}_3\text{Sn}$ bilayer, which was found to be $1754 \Omega^{-1}\text{cm}^{-1}$, from four-point probe measurements. We found σ_{SH} to be $-702 \hbar/e \Omega^{-1}\text{cm}^{-1}$. Zhang *et al.* have predicted an intrinsic SHE in Mn_3Sn that arises due to the non-collinear magnetic structure. They predicted $\sigma_{\text{SH}}^{\text{int}} \approx 90(\hbar/e)\Omega^{-1}\text{cm}^{-1}$ at the Fermi level. Our value is significantly larger and has the opposite sign, which can be explained if we assume the Fermi level is shifted in our thin films due to slightly higher Mn content. In fact, the band structure is found to be dominated by Mn-*d* orbitals near the Fermi level³⁷ and hence, an excess 3% Mn concentration ($\text{Mn}_{3.12}\text{Sn}_{0.88}$) in our samples can induce electron doping leading to a shift in the Fermi level. Such shift in Fermi level is already reported in Mn_3Sn both by first principle calculations as well as by angle-resolved photoemission spectroscopy (ARPES) measurements.³⁷ Based on the mea-

sured resistivity and using a scattering time of 62.3 fs from Ref³⁸, we calculated a shift of about 0.09 eV (w.r.t. stoichiometric Mn_3Sn with no excess Mn) which can easily lead to a sign change in σ_{SH} , as shown in the inset of Fig. 2(f). However, this can not explain the large magnitude of σ_{SH} , indicating that other extrinsic mechanisms may also contribute to σ_{SH} .

In conclusion, we have demonstrated epitaxial growth of *c*-plane oriented non-collinear antiferromagnet Mn_3Sn with Ru as a seed layer on Al_2O_3 substrates. We have investigated ISHE in the *c*-plane $\text{Mn}_3\text{Sn}/\text{Ni}_{80}\text{Fe}_{20}$ system. Through Mn_3Sn thickness dependent ISHE measurements, we determine key parameters like θ_{SH} and $\lambda_{\text{Mn}_3\text{Sn}}$ for *c*-plane Mn_3Sn . We found a large σ_{SH} of $-702 \hbar/e \Omega^{-1}\text{cm}^{-1}$, which is higher than other non-collinear antiferromagnets reported till date. The results are important for spin-orbit torque-based spintronics devices utilizing non-collinear antiferromagnets.

ACKNOWLEDGMENTS

The partial support from the Ministry of Human Resource Development under the IMPRINT program (Grant no: 7519 and 7058), the Department of Electronics and Information

Technology (DeitY), Science & Engineering research board (SERB File no. CRG/2018/001012), Joint Advanced Technology Centre at IIT Delhi, and Department of Science and Technology under the Nanomission program (grant no: *SR/NM/NT – 1041/2016(G)*) are gratefully acknowledged. H.B. gratefully acknowledges the financial support from the Council of Scientific and Industrial Research (CSIR), Government of India.

I. AUTHOR DECLARATIONS

Conflict of Interest

The authors have no conflicts to disclose.

II. DATA AVAILABILITY

The data that support the findings of this study are available from the corresponding author upon reasonable request.

- ¹W. Han, Y. Otani, and S. Maekawa, *npj Quantum Mater.* **3**, 27 (2018).
- ²I. Žutić, J. Fabian, and S. D. Sarma, *Rev. Mod. Phys.* **76**, 323 (2004).
- ³Y. Zhang, J. Železný, Y. Sun, J. Van Den Brink, and B. Yan, *New J. Phys.* **20**, 073028 (2018).
- ⁴O. Busch, B. Göbel, and I. Mertig, *Phys. Rev. B* **104**, 184423 (2021).
- ⁵S. Nakatsuji, N. Kiyohara, and T. Higo, *Nature* **527**, 212 (2015).
- ⁶K. Kondou, H. Chen, T. Tomita, M. Ikhlas, T. Higo, A. H. MacDonald, S. Nakatsuji, and Y. Otani, *Nat. Commun.* **12**, 6491 (2021).
- ⁷M. Ikhlas, T. Tomita, T. Koretsune, M.-T. Suzuki, D. Nishio-Hamane, R. Arita, Y. Otani, and S. Nakatsuji, *Nat. Phys.* **13**, 1085 (2017).
- ⁸T. Higo, H. Man, D. B. Gopman, L. Wu, T. Koretsune, O. M. van't Erve, Y. P. Kabanov, D. Rees, Y. Li, M.-T. Suzuki, *et al.*, *Nat. Photonics* **12**, 73 (2018).
- ⁹H. Chen, Q. Niu, and A. H. MacDonald, *Phys. Rev. Lett.* **112**, 017205 (2014).
- ¹⁰J. Kübler and C. Felser, *EPL* **108**, 67001 (2014).
- ¹¹M. Kimata, H. Chen, K. Kondou, S. Sugimoto, P. K. Muduli, M. Ikhlas, Y. Omori, T. Tomita, A. MacDonald, S. Nakatsuji, *et al.*, *Nature* **565**, 627 (2019).
- ¹²X. Li, C. Collignon, L. Xu, H. Zuo, A. Cavanna, U. Gennser, D. Maily, B. Fauqué, L. Balents, Z. Zhu, *et al.*, *Nat. Commun.* **10**, 1 (2019).
- ¹³Y. Takeuchi, Y. Yamane, J.-Y. Yoon, R. Itoh, B. Jinnai, S. Kanai, J. Ieda, S. Fukami, and H. Ohno, *Nat. Mater.* **20**, 1364 (2021).
- ¹⁴T. Jungwirth, X. Marti, P. Wadley, and J. Wunderlich, *Nat. Nanotechnol.* **11**, 231 (2016).
- ¹⁵V. Baltz, A. Manchon, M. Tsoi, T. Moriyama, T. Ono, and Y. Tserkovnyak, *Rev. Mod. Phys.* **90**, 015005 (2018).
- ¹⁶Y. Zhang, Y. Sun, H. Yang, J. Železný, S. P. P. Parkin, C. Felser, and B. Yan, *Phys. Rev. B* **95**, 075128 (2017).
- ¹⁷P. K. Muduli, T. Higo, T. Nishikawa, D. Qu, H. Isshiki, K. Kondou, D. Nishio-Hamane, S. Nakatsuji, and Y. Otani, *Phys. Rev. B* **99**, 184425 (2019).
- ¹⁸T. Yu, H. Wu, H. He, C. Guo, C. Fang, P. Zhang, K. L. Wong, S. Xu, X. Han, and K. L. Wang, *APL Mater.* **9**, 041111 (2021).
- ¹⁹J. Yoon, Y. Takeuchi, R. Itoh, S. Kanai, S. Fukami, and H. Ohno, *Appl. Phys. Express* **13**, 013001 (2019).
- ²⁰A. Kumar, R. Bansal, S. Chaudhary, and P. K. Muduli, *Phys. Rev. B* **98**, 104403 (2018).
- ²¹P. Deorani and H. Yang, *Appl. Phys. Lett.* **103**, 232408 (2013).
- ²²A. Kumar, N. Pandey, D. Kumar, M. Gupta, S. Chaudhary, and P. K. Muduli, *Physica B: Condensed Matter* **570**, 254 (2019).
- ²³S. Kurdi, P. Zilske, X. Xu, M. Frentrup, M. Vickers, Y. Sakuraba, G. Reiss, Z. Barber, and J. Koo, *J. Appl. Phys.* **127**, 165302 (2020).
- ²⁴T. Higo, D. Qu, Y. Li, C. Chien, Y. Otani, and S. Nakatsuji, *Appl. Phys. Lett.* **113**, 202402 (2018).
- ²⁵T. Ikeda, M. Tsunoda, M. Oogane, S. Oh, T. Morita, and Y. Ando, *AIP Adv.* **10**, 015310 (2020).
- ²⁶Z. Celinski, K. Urquhart, and B. Heinrich, *J. Magn. Magn. Mater.* **166**, 6 (1997).
- ²⁷M. Farle, *Rep. Prog. Phys.* **61**, 755 (1998).
- ²⁸C. Kittel, *Phys. Rev.* **73**, 155 (1948).
- ²⁹O. Gladii, L. Frangou, A. Hallal, R. L. Seeger, P. Noël, G. Forestier, S. Aufferet, M. Rubio-Roy, P. Warin, L. Vila, S. Wimmer, H. Ebert, S. Gambarelli, M. Chshiev, and V. Baltz, *Phys. Rev. B* **100**, 174409 (2019).
- ³⁰A. Conca, B. Heinz, M. Schweizer, S. Keller, E. T. Papaioannou, and B. Hillebrands, *Phys. Rev. B* **95**, 174426 (2017).
- ³¹H. Bangar, A. Kumar, N. Chowdhury, R. Mudgal, P. Gupta, R. S. Yadav, S. Das, and P. K. Muduli, *ACS Appl. Mater. Interfaces*, DOI:<https://doi.org/10.1021/acsami.2c11162> (2022).
- ³²P. Deorani, J. Son, K. Banerjee, N. Koirala, M. Brahlek, S. Oh, and H. Yang, *Phys. Rev. B* **90**, 094403 (2014).
- ³³J. Lustikova, Y. Shiomi, and E. Saitoh, *Phys. Rev. B* **92**, 224436 (2015).
- ³⁴O. Mosendz, J. Pearson, F. Fradin, G. Bauer, S. Bader, and A. Hoffmann, *Phys. Rev. Lett.* **104**, 046601 (2010).
- ³⁵B. B. Singh, K. Roy, J. A. Chelvane, and S. Bedanta, *Phys. Rev. B* **102**, 174444 (2020).
- ³⁶W. Zhang, W. Han, S.-H. Yang, Y. Sun, Y. Zhang, B. Yan, and S. S. Parkin, *Sci. Adv.* **2**, e1600759 (2016).
- ³⁷K. Kuroda, T. Tomita, M.-T. Suzuki, C. Bareille, A. Nugroho, P. Goswami, M. Ochi, M. Ikhlas, M. Nakayama, S. Akebi, *et al.*, *Nat. Mater.* **16**, 1090 (2017).
- ³⁸B. Cheng, Y. Wang, D. Barbalas, T. Higo, S. Nakatsuji, and N. Armitage, *Appl. Phys. Lett.* **115**, 012405 (2019).